ACS OMEGA

http://pubs.acs.org/journal/acsodf

Article

Complex Impedance Analysis on Charge Accumulation Step of Mn_3O_4 Nanoparticles during Water Oxidation

Hongmin Seo,[⊥] Sunghak Park,[⊥] Kang Hee Cho,[⊥] Seungwoo Choi, Changwan Ko, Hyacinthe Randriamahazaka,* and Ki Tae Nam*

Cite This: *ACS Omega* 2021, 6, 18404−18413

Read Online

ACCESS | Metrics & More | Article Recommendations | Supporting Information

ABSTRACT: The development of efficient water-oxidizing electrocatalysts is a key issue for achieving high performance in the overall water electrolysis technique. However, the complexity of multiple electron transfer processes and large activation energies have been regarded as major bottlenecks for efficient water electrolysis. Thus, complete electrochemical processes, including electron transport, charge accumulation, and chemical bond formation/dissociation, need to be analyzed for establishing a design rule for film-type electrocatalysts. In light of this, complex capacitance analysis is an effective tool for investigating the charge accumulation and dissipation processes of film-type electrocatalysts. Here, we conduct complex capacitance analysis for the Mn_3O_4 nanocatalyst, which exhibits superb catalytic activity for water oxidation under neutral conditions. Charge was accumulated on the catalyst surface by the change in Mn valence between Mn(II) and Mn(IV) prior to the rate-determining O−O bond forming step. Furthermore, we newly propose the dissipation ratio (D) for understanding the energy balance between charge accumulation and charge consumption for chemical O−O bond formation. From this analysis, we reveal the potential- and thickness-dependent contribution of the charge accumulation process on the overall catalytic efficiency. We think that an understanding of complex capacitance analysis could be an effective methodology for investigating the charge accumulation process on the surface of general film-type electrocatalysts.

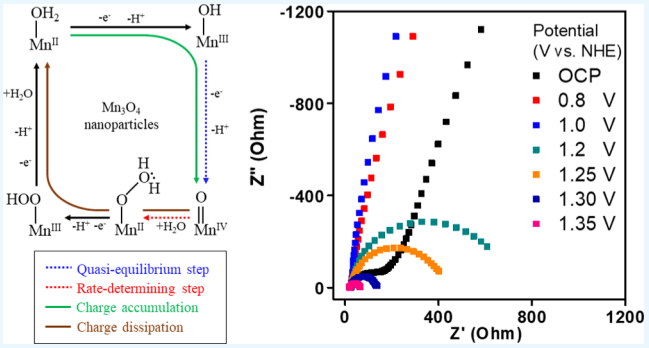

INTRODUCTION

Electrochemical water splitting has been regarded as an attractive approach to attain sustainable energy system by producing clean hydrogen energy without the formation of undesirable byproducts.[1−3] Substantial research efforts have been devoted to the practical application of water electrolysis technology to obtain environmentally friendly hydrogen energy. However, the sluggish kinetics of the anodic half reaction, the oxygen evolution reaction (OER), are a major obstacle to improving the overall performance of water electrolysis.[3] Owing to their high performance and stability, noble-metal-based catalysts such as RuO_X and IrO_X have generally been utilized, but their high cost and scarcity have limited their scalable application.[4,5] In this regard, numerous first-row transition-metal-oxide (TMO)-based catalysts have been developed to achieve superb activity that is comparable to that of noble-metal-based catalysts.[6−10]

For achieving the optimal catalytic performance strategically, the key descriptors have been studied for the OER electrocatalysts. The binding affinity with oxygen species such as O*, HO*, and HOO* on the catalyst surface has been regarded as an important determinant for the catalytic activity.[11] From density functional theory (DFT) studies, a scaling relation between the binding energy of HO* and HOO* species has been found for general metal-oxide-based electrocatalysts. The scaling relation constructed a volcano-type trend between the catalytic activity and the difference in binding energies of O* and HO* ($\Delta G_{O*} - \Delta G_{HO*}$).[11] Additionally, for perovskite-based electrocatalysts, occupancy of the e_g orbital of the surface metal cation has been suggested as another descriptor for the OER activity, as the e_g orbital participated in σ bonding with anionic adsorbates.[12] An e_g occupancy close to unity is the optimal electronic configuration for the lowest OER overpotential.

In the volcano-type trend for OER overpotential, a discrepancy between the theoretical and experimental values has been observed under neutral pH conditions. Specifically, DFT studies using $\Delta G_{O*} - \Delta G_{OH*}$ as a descriptor have predicted that 3d TMO-based catalysts, such as Co_3O_4, NiO,

Received: May 7, 2021
Accepted: June 24, 2021
Published: July 6, 2021

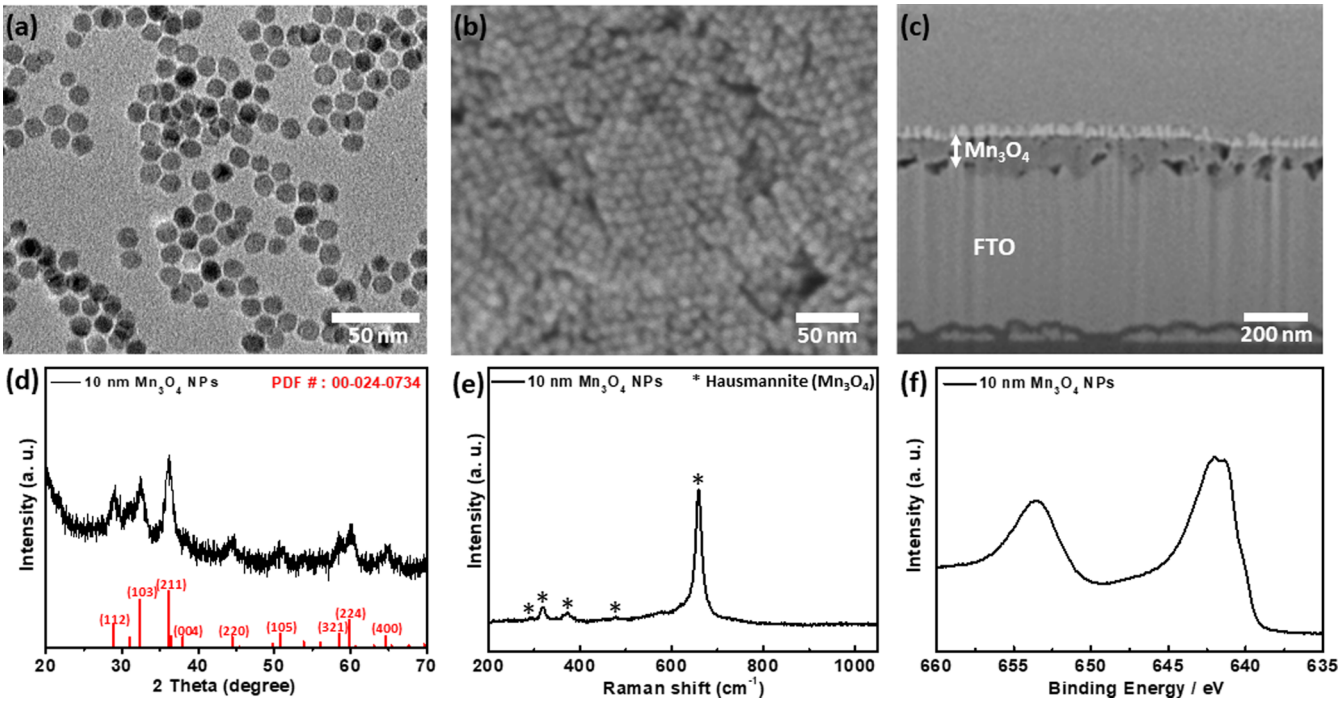

Figure 1. Characterization of the as-synthesized 10 nm Mn_3O_4 NPs. (a) TEM image of the monodispersed Mn_3O_4 NPs. (b) Plane SEM image for 300 nm-thickness Mn_3O_4 NP film. (c) Cross-sectional SEM image of the Mn_3O_4 NP films on the FTO substrate. (d) PXRD pattern, (e) Raman spectrum, and (f) Mn 2p XPS spectrum of the Mn_3O_4 NPs.

and MnO_X, have similar overpotentials to that of IrO_X.[11,13] Experimentally, the overpotential value for Mn_3O_4 is hundreds of millivolts higher than that of IrO_X. The discrepancy between the experimental and theoretical values originated from the overly simplified descriptor used in theoretical analysis.[14] Therefore, it is important to analyze various parameters including kinetic factors during the electrochemical water oxidation reaction process.

The morphology and thickness of film-type electrocatalysts significantly affect their overall OER performance. Specifically, the high porosity of a catalyst film contributes to an increase in its surface area and this is related to the activity enhancement because of the increased number of active sites. Also, catalyst films exhibit the best activity when at an optimal thickness.[15−17] This thickness-dependent trend has been explained by competition between the increase in the number of active sites and the electron transport resistance through the catalyst film. Additionally, the interfacial band structure between the catalyst and the bottom electrode must be considered for facile electron transport.[18]

In addition to structural features affecting the performance of a catalyst film, the charge accumulation property also greatly influences the OER efficiency of film-type electrocatalysts. The electrochemical OER involves several chemical elementary steps such as O−O bond formation.[19] The O−O bond formation proceeds through the nucleophilic attack of water molecules[20] or radical coupling of adjacent metal−oxo species,[21] where the chemical bond formation/dissociation occurs entailing a valence state change of the metal center on the active site. Prior to the O−O bond formation step, an oxidative charge is accumulated with the metal valence change on the metal-oxide-based electrocatalysts.[22] Thus, charge accumulation needs to be evaluated among the various electrochemical processes to understand the rate-controlling process of the electrochemical OER. Although there are different reports on the rate-determining step (RDS) of IrO_X,[23] the low-spin configuration of Ir enables efficient charge accumulation under neutral pH conditions.[24] In contrast, MnO_2 electrocatalyst suffers from inefficient charge accumulation under neutral pH conditions due to the charge disproportionation of high-spin Mn(III) species.[24] In light of this, for an advanced design rule for OER electrocatalysts, the charge accumulation process should be understood at the interface between the catalyst surface and the electrolyte during the electrochemical OER.

In this regard, manganese is particularly an interesting candidate due to its various oxidation states from Mn(II) to Mn(VII)[25] and the selected element in biological water-oxidizing complex in photosystem II.[26,27] The high efficiency of the biological water-oxidizing complex under mild conditions is attributable to its dynamic and asymmetric structure which enables efficient charge accumulation and subsequent O−O bond formation. Charge accumulation is promoted by stepwise oxidation from Mn(III) to Mn(IV) for the Mn_4CaO_5 cluster in the water-oxidizing complex during the Kok cycle.[28] The activity of synthetic Mn-based electrocatalysts under mild conditions is markedly degraded compared to that observed under alkaline conditions due to the instability of the Mn(III) species on the surface. The Mn(III) species on the surface of crystalline manganese oxides undergo charge disproportionation under neutral and acidic conditions.[29] Inducing a local structural distortion or structural disordering is reported as effective strategies to stabilize the surface Mn(III) species and enhance the OER activity under neutral conditions.[30−33]

We have previously developed sub-10 nm-sized manganese oxide nanocatalysts, which exhibited good OER activity under neutral conditions.[34,35] Combined with *in situ* spectroscopic analysis (X-ray absorption, UV−vis, and Raman spectroscopy) and electrokinetic studies, we revealed their unique reaction

https://doi.org/10.1021/acsomega.1c02397
ACS Omega 2021, 6, 18404−18413

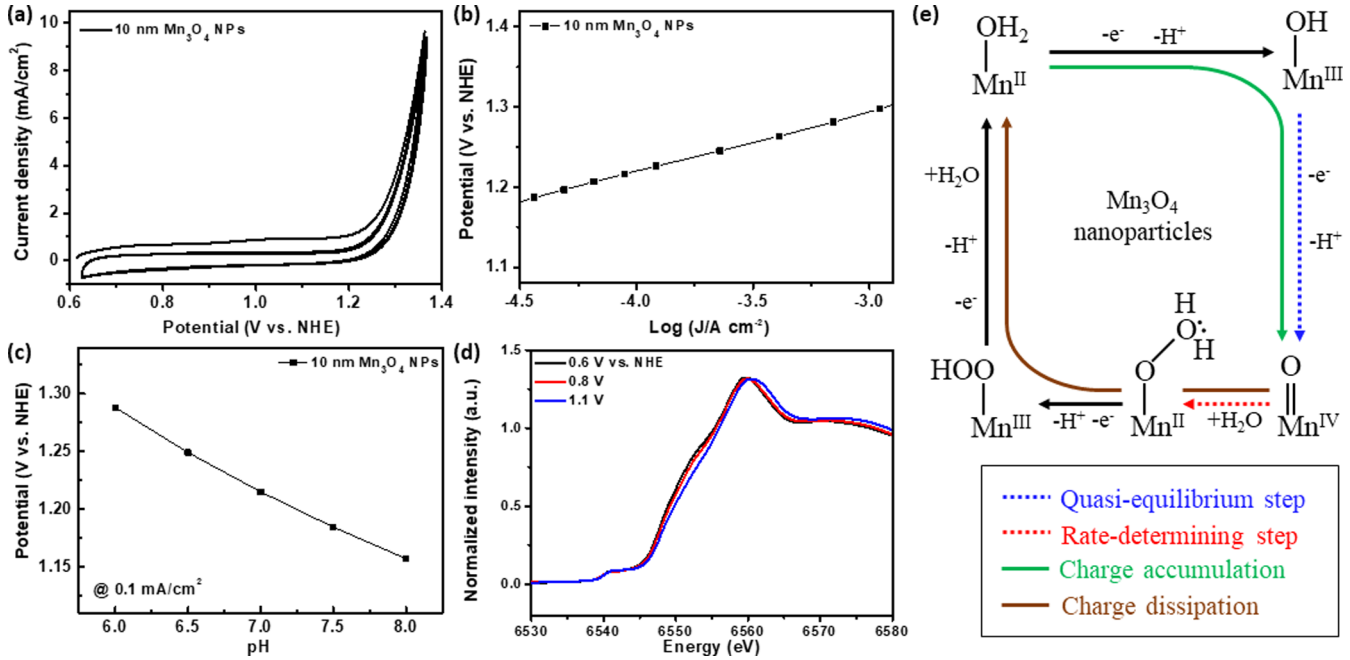

Figure 2. Electrochemical kinetic analyses of the Mn_3O_4 NPs. (a) CV curve for 70 nm-thickness Mn_3O_4 NP electrode in 0.5 M phosphate buffer solution (pH 7). (b) Tafel plot in 0.5 M phosphate buffer solution (pH 7). (c) pH dependency over neutral range from a pH of 6.0 to 8.0 in 0.5 M phosphate buffer solution. (d) Mn K-edge *in situ* XANES spectra of the Mn_3O_4 NPs at different anodic potential in 0.5 M phosphate buffer solution (pH 7). (e) Proposed OER mechanism on the Mn_3O_4 NPs under neutral conditions.

mechanism which was totally different from that of the bulk crystalline manganese oxide electrocatalysts.[36] The RDS is the chemical O−O bond formation where Mn(IV)═O species are involved in ref 37. It was indicated that the charge accumulation process was facilitated *via* an Mn valence change prior to the O−O bond formation step. Furthermore, the electron transport characteristics for a manganese oxide nanocatalyst film were analyzed *via* electrochemical impedance spectroscopy (EIS) using a newly modified transmission line model.[38] From this EIS study, the overall catalytic performance was determined by the competition between charge transport and surface catalysis.

Here, we investigate the charge accumulation behavior on a manganese oxide nanoparticle (NP) film during the OER *via* complex capacitance analysis from an EIS study. For general complex capacitance analysis of capacitors and pseudocapacitors, the real (C') and imaginary (C'') capacitance indicate the charging property and energy dissipation process, respectively. From this viewpoint, complex capacitance analysis could decouple the electrochemical oxidative charge accumulation process and oxidative charge consumption process during the OER. Also, we newly propose the dissipation ratio to describe the ration of energy balance between the charge accumulation and consumption processes. The potential-dependent change for these parameters provides insights into charge accumulation on heterogeneous electrocatalysts during the OER.

RESULTS AND DISCUSSION

Characterization of the Mn_3O_4 NPs. Uniform spherical sub-10 nm Mn_3O_4 NPs were successfully synthesized by the hot-injection method (Figure 1a). The electrode film was prepared through the spin coating of the as-prepared Mn_3O_4 NPs ink solution onto the FTO substrate. As shown in Figure 1b,c, the Mn_3O_4 NPs were well-assembled onto the FTO substrate. The thickness of the electrode was precisely controlled from 20 to 300 nm by changing the concentration of Mn_3O_4 NP ink solution (Figure 1b,c and S1). As shown in Figure 1d, the powder X-ray diffraction (XRD) spectrum of our NPs well match with the Mn_3O_4 phase (PDF#: 00-024-0734). In addition, the spectra of the Raman spectroscopy analysis clearly demonstrate the characteristic Raman bands of spinel Mn_3O_4 (hausmannite) at the peak position of 290, 320, 373, 479, and 659 cm^{-1} (Figure 1e).[37,39] The peak position of both Mn $2p_{3/2}$ and Mn $2p_{1/2}$ peaks are located at 641.57 and 653.5 eV (Figure 1f), which matches well with previous studies of Mn_3O_4.[35,40]

Electrochemical Kinetic Analyses of Mn_3O_4 NPs. Figure 2a illustrates the cyclic voltammetry (CV) curves of the Mn_3O_4 NPs under 0.5 M phosphate buffer solution (pH 7). The CV curves of the Mn_3O_4 NPs indicate that the Mn_3O_4 NPs are active for electrochemical OER, showing the drastic catalytic current increase above 1.2 V *versus* NHE. Furthermore, we observed the stable water-oxidizing electrocatalytic activity of the Mn_3O_4 NPs under the phosphate electrolyte (Figure S2). The confirmation of an Mn phosphate overlayer is an important point to ensure the composition of the real catalyst during the water oxidation reaction in the phosphate electrolyte.[41] The P 2p XPS data of the spent electrocatalyst indicate that there is no formation of Mn phosphate overlayer on our Mn_3O_4 NP sample. Additional Mn 2p XPS, Raman, transmission electron microscopy (TEM), and scanning electron microscopy (SEM) characterization confirmed that the morphology and size of the Mn_3O_4 NPs remained unchanged after the electrolysis and only slight oxidation of the Mn_3O_4 NPs was observed (Figures S3 and S4).

In addition, Tafel and pH dependency analyses were performed to investigate the electrokinetic behavior of the Mn_3O_4 NPs (Figure 2b,c). The Tafel plots were obtained from chronoamperometry methods. The measured Tafel slope of

https://doi.org/10.1021/acsomega.1c02397
ACS Omega 2021, 6, 18404−18413

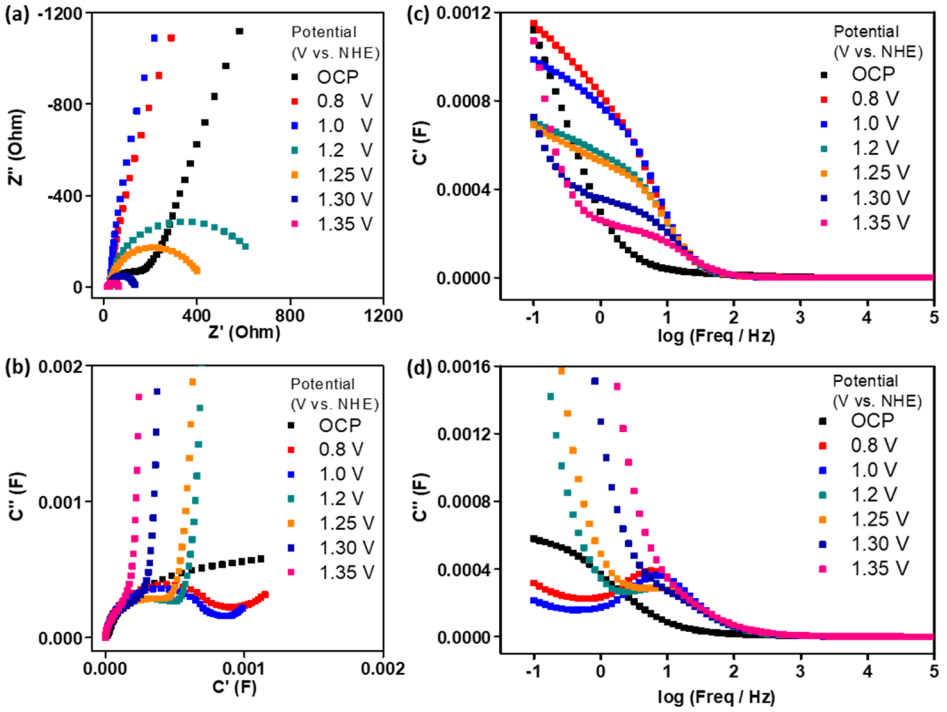

Figure 3. Impedance plots for 70 nm-thickness Mn_3O_4 NP film at OCP, 0.8, 1.0, 1.2, 1.25, 1.3 and 1.35 V *vs* NHE. (a) Nyquist plot (Z' *vs* Z''). (b) Complex capacitance plot (C' *vs* C''). (c) Real part (C') for complex capacitance as a function of frequency. (d) Imaginary part (C'') for complex capacitance as a function of frequency.

72.8 mV dec^{-1} in the Mn_3O_4 NPs corresponds to the apparent transfer coefficient (α) of 0.81, which approximately corresponds to the chemical RDS with one-electron transferring pre-equilibrium step.[36,42] In addition, the pH dependency of the Mn_3O_4 NPs against the current density was investigated and measured to be −65.3 mV per pH (Figure 2c). From the Tafel and pH dependence analyses, the first-order dependency of log(j) on pH can be derived. Combining the electrokinetic results, we can conclude that the one proton (H^+) and one electron (e^-) transfer occurs as the quasi-equilibrium step.[43] Furthermore, we recently observed the Mn(IV)═O intermediates on the surface of the same Mn_3O_4 NP electrocatalyst during the electrochemical water oxidation by *in situ* Raman analysis.[37]

Taken together, based on the aforementioned electrokinetic studies and previously investigated *in situ* spectroscopic analyses,[36,37] we could propose the following mechanism which is summarized in Figure 2e. During the catalytic cycle, the active Mn species were oxidized from Mn(II) to Mn(IV). The Mn(III) species, regarded as the key species for the OER activity under neutral conditions, were also stabilized on the surface of the small-sized nanoparticle. Then, a concerted one proton (H^+) and one electron (e^-) transfer takes place as the quasi-equilibrium step, resulting in the generation of Mn-(IV)═O species. Following the quasi-equilibrium step, formation of an O−O bond at the Mn(IV)═O species proceeded as the RDS for the surface catalysis with a decrease in Mn valence state. Oxygen molecules were liberated and the water molecule was adsorbed on the active site in the subsequent process. In the proposed mechanism, the Mn valence showed a reversible change with chemical bond rearrangement, indicating that the electrochemical OER could be a complementary process with charge accumulation and dissipation of the electrocatalyst.

As shown in Figures 2a and S5, the CV curves were measured for a 20, 70, 150, and 300 nm-thick Mn_3O_4 NP films under 0.5 M phosphate buffer solution of pH 7. The electrode has a porous structure in which the Mn_3O_4 NPs are compactly assembled. Therefore, the surface area increases as the thickness of the sample increases, resulting in an increase of capacitance currents and the OER electrocatalytic activities (Figures S5 and S6). The rectangular capacitive shape without a noticeable redox peak is very similar with that of the previously reported Mn_3O_4 samples, which mainly originated from the faradaic pseudocapacitance by the redox state change of Mn.[44,45] The valence state change of Mn center in the Mn_3O_4 NPs according to the applied potential is directly supported by the potential-dependent *in situ* XANES data (Figures 2d and S7).

Complex Capacitance Analysis for Mn_3O_4 NPs. We conducted EIS analysis to understand the charge accumulation process of the Mn_3O_4 NP films during catalysis. EIS analysis is an effective tool for decoupling various electrochemical processes. We previously parameterized electron transport and surface catalysis in the Mn_3O_4 NP films using the proposed circuit model.[38] Herein, we understand the charge accumulation and dissipation processes from impedance data (Z^*) which can be converted into complex capacitance (C^*) *via* the following equations (eqs 1 and 2).

$$C^*(w) = \frac{1}{jwZ^*(w)} \tag{1}$$

$$C^*(w) = C'(w) - jC''(w) \tag{2}$$

In eqs 1 and 2, w, j, C', and C'' are the frequency, imaginary unit, real capacitance, and imaginary capacitance, respectively. The real (C') and imaginary (C'') capacitances were calculated

https://doi.org/10.1021/acsomega.1c02397
ACS Omega 2021, 6, 18404−18413

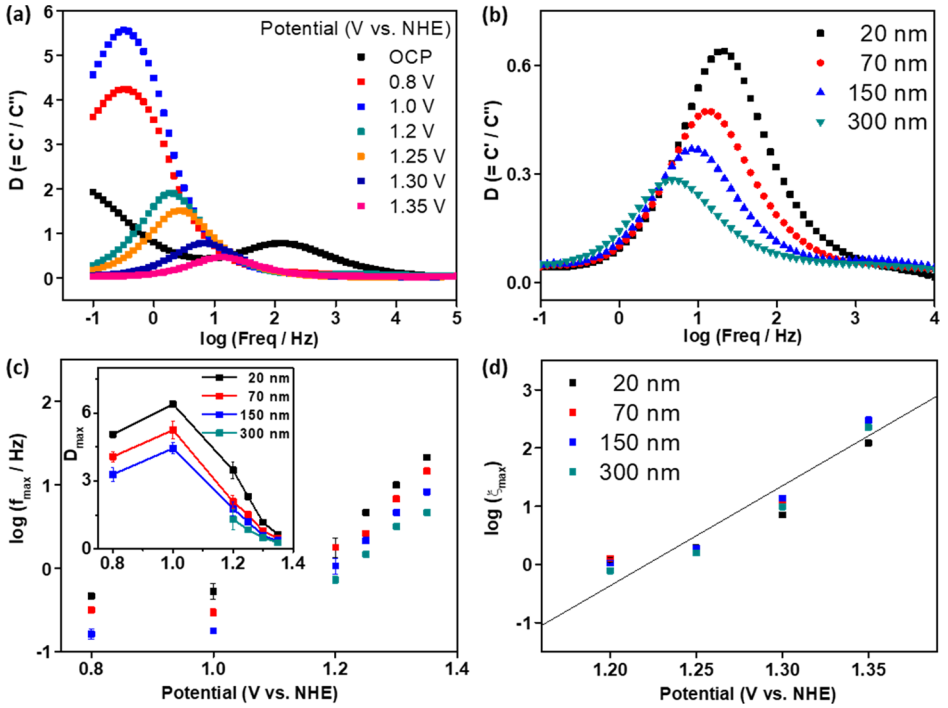

Figure 4. (a) Dissipation ratio (C'/C'') as a function of frequency for 70 nm-thickness film at OCP, 0.8, 1.0, 1.2, 1.25, 1.3 and 1.35 V *vs* NHE. (b) Dissipation ratio (C'/C'') as a function of frequency at 1.35 V *vs* NHE with 20, 70, 150, and 300 nm-thickness films. (c) Peak frequency (f_{max}) and dissipation ratio (D_{max}) at f_{max} variance as a function of potential. (d) Corrected peak frequency $(\log(\xi_{max}) = \log(f_{max})/D_{max})$ for 20, 70, 150 and 300 nm-thickness films.

from the real (Z') and imaginary (Z'') impedances according to eqs 3 and 4.

$$C'(w) = \frac{Z''(w)}{w|Z(w)|^2} \tag{3}$$

$$C''(w) = \frac{-Z'(w)}{w|Z(w)|^2} \tag{4}$$

Complex capacitance analysis has previously been utilized to investigate the capacitive characteristics of various energy materials.[46−51] Complex capacitance analysis is an effective tool for understanding the capacitive response at low frequency range, whereas the impedance spectra generally concentrate on the analysis of the resistive behavior at a higher frequency range. The real capacitance represents the ability of the system to store electrical energy and the imaginary capacitance indicates losses in the form of energy dissipation. For an OER electrocatalyst system, the real capacitance can be interpreted as the energy storage ability by the oxidative charge accumulation by Mn valence state change, and the imaginary capacitance is related to the energy losses by oxidative charge consumption with chemical bond rearrangement such as O−O bond formation. In this regard, complex capacitance analysis can show the energy balance between charge accumulation and charge dissipation for the OER on the Mn_3O_4 NP films.

We obtained EIS measurements for the Mn_3O_4 NP films in 0.5 M PBS at pH 7 between the open circuit potential (OCP) and 1.35 V *versus* NHE. As shown in Figures 3a and S8, impedance data for the Mn_3O_4 NPs were displayed as a Nyquist plot (Z' *vs* Z''). In the impedance spectra at the OCP, a semicircle and curve with a low curvature were observed at higher and lower frequency ranges, respectively. The curve at the low frequency range indicated the electrochemical processes at the interface between the catalyst and electrolyte, and the semicircle at the high frequency range was related to the electron transport behavior through the catalyst film and the charge transfer process at the interface between the catalyst and the bottom electrode. As the applied potential was increased, the semicircle shape disappeared and only the curve with the low curvature was observed at 0.8 and 1.0 V *versus* NHE. Above 1.2 V *versus* NHE, a new semicircle emerged, which corresponds to the OER on the catalyst surface. The size of the semicircles reduced as the potential was increased from 1.2 to 1.35 V *versus* NHE. The change in the spectra with increasing potential was attributable to the decrease in interfacial charge transfer resistance for the OER.

The complex capacitance values were converted from the impedance data using eqs 3 and 4 to analyze the charge accumulation process in the Mn_3O_4 NP films during the OER (Figures 3b and S9). Additionally, the real and imaginary parts of the complex capacitance were plotted as a function of frequency on a log scale (Figure 3c,d). As shown in Figure 3c,d, the values for C' and C'' were zero above approximately 10^2 Hz. This resistive behavior indicated that charge was difficult to be accumulated and the energy dissipation process was inhibited at a higher frequency. At a lower frequency range ($<10^2$ Hz), the capacitive behavior showed an increase in C' (Figure 3c). As shown in Figure 3d, a capacitive peak and an energy dissipative tail indicated that the charge accumulation and energy dissipation processes were complementary interactions during the OER on the electrocatalyst film.

At the OCP, C' increased below 10^0 Hz and a capacitive peak in the log f *versus* C'' plot was observed at around 10^{-1} Hz. This was attributed to the formation of an electrical double layer near the catalyst surface. At 0.8 V *versus* NHE, an increase

https://doi.org/10.1021/acsomega.1c02397
ACS Omega 2021, 6, 18404−18413

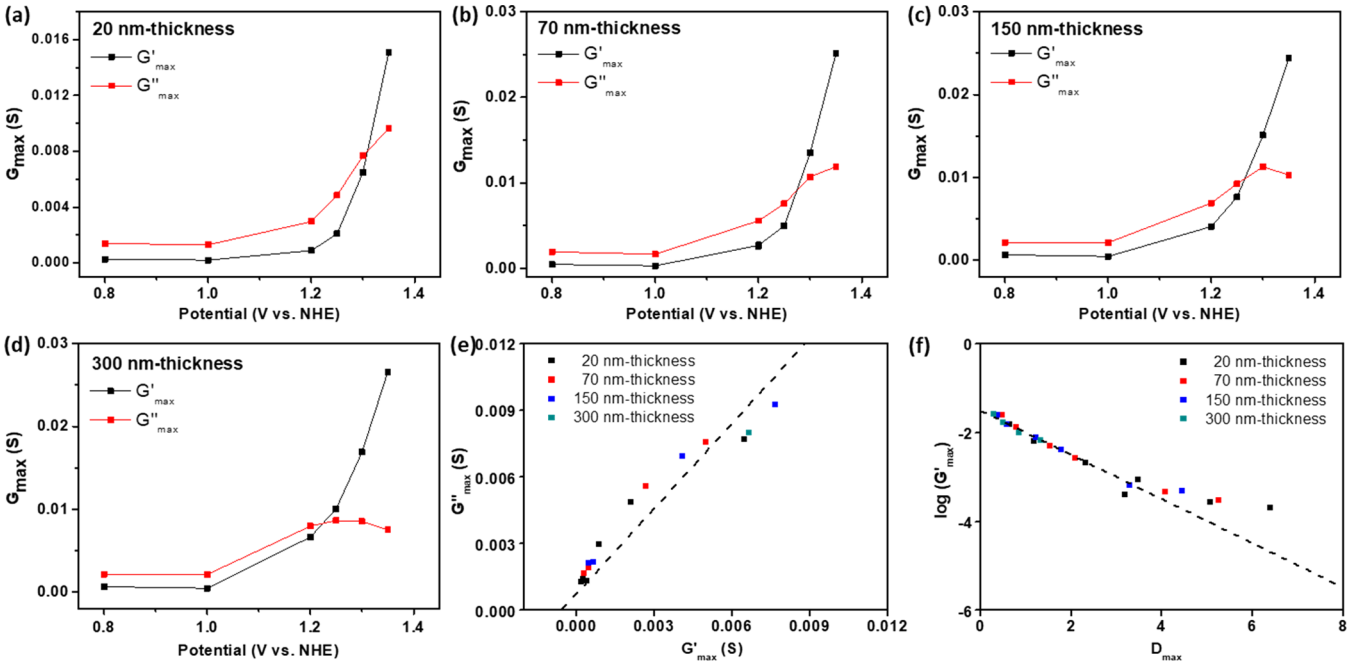

Figure 5. Real conductance (G'_{max}) and imaginary conductance (G''_{max}) at peak frequency (f_{max}) for (a) 20, (b) 70, (c) 150, and (d) 300 nm-thickness Mn_3O_4 NPs electrodes. (e) Correlation between G'_{max} and G''_{max} for various electrode thicknesses where G' is lower than G'' ($G' < G''$). (f) Variation of G'_{max} as a function of the dissipation ratio at the peak frequency (f_{max}).

in C' was observed at under ~10^2 Hz and the slope for C' changed at around $10^{0.33}$ Hz (Figure 3c). In Figure 3d, the capacitive peak was positively shifted to 10^1 Hz. This change in the spectra was attributed to the charge accumulation with the Mn valence change between Mn(II), Mn(III), and Mn(IV) on the Mn_3O_4 NP surface. At 1.0 V *versus* NHE, the increase in C' was reduced slightly at a lower frequency range (<$10^{0.33}$ Hz) and the capacitive peak frequency was nearly unchanged (Figure 3d).

Above 1.0 V *versus* NHE, a substantial decrease in the rate of increase in C' was observed at the lower frequency range (<10 Hz, Figure 3c). Also, dissipative tails emerged in the lower frequency range, which represented the charge dissipation process on the catalyst surface by oxygen-evolving catalysis (Figure 3d). The change in the spectra indicated that water oxidation reaction including the chemical O−O bond formation step was initiated at this potential range, where Mn(III)−OH and Mn(IV)═O species were sufficiently generated on the Mn_3O_4 NP surface (Figure 2a). The dissipative tail was positively shifted as the potential was increased from 1.2 to 1.35 V *versus* NHE, which indicates that the OER proceeded briskly at a higher potential. Additionally, above 1.3 V *versus* NHE, the slope for C' became steeper at a frequency range less than 10^0 Hz, which was attributed to the electron transport limitation in the film-type electrocatalyst.

From the complex capacitance analysis, the increase of the real part in the low frequency range indicated that charge was accumulated by the Mn valence change on the Mn_3O_4 NP surface below 1.2 V *versus* NHE. Above 1.2 V *versus* NHE, the real part decreased and the dissipative tail was observed in the imaginary part of the plot in the lower frequency range. The change in the spectra signifies that the accumulated charge was consumed to continue the further steps of the OER (Figure 2e). In this regard, the complex capacitance analysis demonstrated an energy balance between the oxidative charge accumulation and dissipation processes on the Mn_3O_4 NPs during the OER.

Furthermore, we introduced here the frequency-dependent dissipation ratio (D), which is calculated as the ratio of C' and C'', for analyzing the correlation between the energy balance and the various electrochemical processes on the Mn_3O_4 NP films during the OER (eq 5).

$$D(f) = \frac{C'(f)}{C''(f)} \tag{5}$$

The dissipation ratio (D) indicated the ratio of charge accumulation ability with respect to the dissipation processes. As shown in Figure 4a, the dissipation ratios were plotted as a function of frequency on a log scale at several applied potentials. We found that the dissipation ratio was maximized (D_{max}) at a specific frequency (f_{max}) in each spectrum (Figure 4a). For 1.0 V *versus* NHE and below, D_{max} increased and f_{max} was not significantly changed as the potential rose. The values for D_{max} were measured as 4.2 and 5.6 at 0.8 and 1.0 V *versus* NHE, respectively. The f_{max} values were estimated as $10^{-0.5}$ Hz. The increase in D_{max} was attributed to the charge accumulation being superior to the energy dissipation process with the Mn valence change (Figure 2e). Above 1.0 V *versus* NHE, where Mn(III)−OH and Mn(IV)═O species had been sufficiently generated, D_{max} decreased and f_{max} was positively shifted with increasing potential. The values for D_{max} were 1.91, 1.52, 0.79, and 0.47 at 1.2, 1.25, 1.3 and 1.35 V *versus* NHE, respectively. The respective f_{max} values were measured as $10^{0.25}$, $10^{0.5}$, $10^{0.83}$and $10^{1.17}$ Hz. The decrease in D_{max} represents that the influence of oxidative charge consumption becomes dominant. The increase in f_{max} was due to the increase in the dissipation process kinetics as the potential increased above 1.2 V *versus* NHE (Figure 4c).

In Figure 4b, the dissipation ratios were measured for 20, 70, 150 and 300 nm-thick Mn_3O_4 NP films at 1.35 V *versus* NHE.

https://doi.org/10.1021/acsomega.1c02397
ACS Omega 2021, 6, 18404−18413

As the thickness of the Mn_3O_4 NPs film increased, D_{max} and f_{max} concomitantly decreased. At 1.35 V *versus* NHE, the D_{max} values were measured as 0.64, 0.47, 0.37 and 0.28 for 20, 70, 150, and 300 nm thicknesses, respectively. The corresponding values for f_{max} were $10^{1.33}$, $10^{1.08}$, $10^{0.92}$, and $10^{0.67}$ Hz. The decrease in D_{max} was due to the enhancement of the dissipation process and surface catalysis for the porous Mn_3O_4 NP electrodes. The decrease in f_{max} reflected that the kinetics for the overall OER were slower for thicker Mn_3O_4 NP films due to an increased electron transport limitation under high anodic potential condition.

We further introduced the corrected peak frequency (ξ_{max}) here to rationalize the influence of both the potential and the electrode thickness. The values for ξ_{max} were calculated using the following equation (eq 6).

$$\xi_{max} = \frac{f_{max}}{D(f_{max})} \tag{6}$$

The ξ_{max} value does not vary with the electrode thickness but log ξ_{max} linearly increased with the applied potential above 1.2 V *versus* NHE (Figure 4d). Assuming that the relaxation processes follow the Butler−Volmer formalism, we could propose charging−dissipation-coupled coefficient (α_{c-d}) by the following equation (eq 7), where F, T, and E are the Faraday constant, temperature, and applied potential, respectively. Since the ξ_{max} value is related to the overall kinetics of the charging and dissipation processes, we expect that the α_{c-d} value could provide information about the overall rate-determining kinetic step, such as the apparent transfer coefficient obtained through Tafel analysis. The α_{c-d} was calculated as 0.78 using this equation. The values for α_{c-d} matched well with the transfer coefficient which was measured from Tafel analysis in the previous study.[35,36]

$$\alpha_{c-d} = \left(\frac{RT}{F}\right)\left(\frac{d \ln (\xi_{max})}{dE}\right) \tag{7}$$

Complex Conductance (G' and G'') Analysis for Mn_3O_4 NPs. To analyze the competition between the dissipation process and charge accumulation, complex conductance was converted from complex capacitance using eqs 8 and 10. The complex conductance data were plotted at various applied potentials for several film thicknesses (Figure S10). Figure 5a−d shows potential dependency of the real (G'_{max}) and imaginary (G''_{max}) conductance at the peak frequency (f_{max}). Both G'_{max} and G''_{max} increased with the applied potential for all thicknesses (~20−300 nm), although G''_{max} reaches a plateau at high potential for 150 and 300 nm-thick films. In the low potential range, G'_{max} was lower than G''_{max} and a crossover between G'_{max} and G''_{max} was observed for each film thickness. At a lower potential, G'_{max} is smaller than G''_{max} for each film thickness, which indicated that the charge accumulation process with the Mn valence change was dominant. When G'_{max} is larger than G''_{max}, the dissipation process became dominant during the electrochemical OER.

$$G^*(w) = G'(w) + jG''(w) \tag{8}$$

$$G'(w) = wC''(w) \tag{9}$$

$$G''(w) = wC(w) \tag{10}$$

In Figure 5e, G'_{max} and G''_{max} showed a linear relationship when G'_{max} is smaller than G''_{max}. The smaller values for G'_{max} compared to G''_{max} represented that the Mn valence change process served as a rate-controlling factor for overall efficiency. Importantly, the slope for G''_{max} with respect to G'_{max} was measured as nearly unity, as shown in eq 11.

$$G''_{max} = 1.05G'_{max} + 0.0016 \tag{11}$$

This indicated that the charge accumulation process of the Mn valence change and the dissipation process were strongly correlated with the dissipation process of electron transfer. In other words, this behavior indicates the readiness for Mn valence changes and describes the oxidative charge accumulation with proton release for electroneutral chemical storage of charges, in contrast to an electrostatic capacitor with charge separation. It reflected that the energies from the dissipation process and charge accumulation was balanced, which was caused by the one proton−one electron coupled transfer process prior to the O−O bond-formation step. Also, the intercept of G''_{max} (~0.0016 S) can be viewed as a measure of the energy accumulation threshold beyond which the dissipation processes occur.

Log G'_{max} showed a linear relationship with respect to D_{max} (Figure 5f) for all Mn_3O_4 NP film thicknesses. The intercept was measured as 0.03 S when D_{max} is zero. From eqs 5 and 9, this intercept, G'_{lim}, corresponded to the hypothetical situation where the real capacitance (C', energy storage ability) was zero and the imaginary capacitance (C'', dissipation process) was an infinite value. We emphasize that only one curve was obtained from all the film thicknesses. Hence, G'_{lim} is a useful parameter which reflects the kinetics of the overall electrochemical system, such as the turnover frequency. It can be measured directly from EIS analysis without identifying the number of active sites and using an equivalent circuit model.

CONCLUSIONS

We conducted complex capacitance analysis for the Mn_3O_4 NP films to understand the charge accumulation process on the catalyst surface during the OER. From this complex capacitance analysis, charge was accumulated on the catalyst surface by the change in Mn valence between Mn(II) and Mn(IV) below 1.2 V *versus* NHE. Above 1.2 V *versus* NHE, the accumulated charge was used up by oxygen-evolving catalysis. We newly proposed the dissipation ratio as the ratio of the real capacitance with respect to the imaginary capacitance for analyzing the energy balance between the charge accumulation process and charge dissipation for a catalytic reaction. The potential dependence of the dissipation ratio indicated that the charge dissipation process was superior to charge accumulation at a higher potential. Additionally, the thickness dependence of the dissipation ratio indicated that an electron transport limitation induced charge accumulation on the catalyst surface for thicker catalyst films. We believe that this complex capacitance analysis using EIS could be generalized for various film-type electrocatalysts to investigate the charge accumulation processes on the catalyst surfaces.

EXPERIMENTAL SECTION

Materials. $Mn(CH_3COO)_3{\cdot}2H_2O$ (97%), 1-octadecene (90%), myristic acid ($CH_3(CH_2)_{12}COOH$) (99%), decanol ($CH_3(CH_2)_9OH$), $Na_2HPO_4{\cdot}7H_2O$ (ACS reagent, 98.0−102.0%), and $NaH_2PO_4{\cdot}2H_2O$ (99.0%) were purchased from Sigma-Aldrich and used as received without further purification. Fluorine-doped-tin-oxide-coated glass (FTO, TEC-8)

https://doi.org/10.1021/acsomega.1c02397
ACS Omega 2021, 6, 18404−18413

with the surface resistivity of 15 Ω sq^{-1} was manufactured by Pilington Company.

Synthesis of the Manganese Oxide NPs. The Mn_3O_4 NPs were synthesized by slightly modifying a previously reported method called the hot injection method.[32] To synthesize monodispersed sub-10 nm-sized NPs, 1 mmol manganese acetate and 2 mmol myristic acid were dissolved in 20 mL of octadecene and a mixture of 1.83 mL of decanol and 3 mL of octadecene was prepared. These two separate solutions were degassed at 110 °C for 2 h with stirring. After 2 h of degassing, the solution of manganese acetate and myristic acid was slowly heated up to 290 °C under an argon atmosphere. When the temperature reached above 285 °C, the 1.2 mL mixture of decanol and octadecene was injected rapidly into the solution of manganese acetate and myristic acid. The mixture was maintained at 290 °C for 1 h.

Electrode Preparation. After the synthesis of the Mn_3O_4 NPs in octadecene, the solution of Mn_3O_4 NPs, toluene, and acetone were mixed in the volume ratio of 1:1:2 and centrifuged to precipitate the Mn_3O_4 NPs. This step was repeated three times. Then, the precipitate of Mn_3O_4 NPs was dispersed in hexane. Then, 40 μL of the Mn_3O_4 NP solution was spin-coated onto the FTO substrates at a spin rate of 2000 rpm and a holding time of 10 s. The thickness of the Mn_3O_4 NP films spin-coated on the FTO substrates was controlled by the volume ratio of the initial dark brown Mn_3O_4 NP solution to hexane. To eliminate the organic ligands on the surface of the Mn_3O_4 NPs, the spin-coated film on the FTO substrates were annealed at 300 °C for 5 h.

Scanning Electron Microscopy. The morphology of the Mn_3O_4 NP films on the FTO substrates was characterized with a high resolution scanning electron microscope (SUPRA 55VP, Carl Zeiss, Germany). Images were taken with an acceleration voltage of 2 kV.

X-ray Diffraction. The XRD analysis of Mn_3O_4 NP powder was conducted using an X-ray diffractometer (New D8 ADVANCE, Bruker) with a Cu Kα radiation (λ = 1.5406 Å). The XRD pattern of Mn_3O_4 NPs was measured from 15 to 75° with a step of 0.02.

Raman Spectroscopy. The Raman experiment was conducted with a Raman spectrometer (LabRAM HR Evolution, Horiba) with a 50× long working distance visible objective. The wavenumber of the excitation light source was 532 nm. To make sure of the reliability of the acquired spectrum, the Raman shift was calibrated using a silicon standard sample (520.6 cm^{-1}). The Raman spectrum was obtained with an acquisition time of 120 s with a 600 g/mm grating.

X-ray Photoelectron Spectroscopy. XPS spectra were obtained with a photoelectron spectrometer (K-Alpha+, Thermo Fisher Scientific) using the Al K-Alpha source with a pass energy of 40 eV and step size of 0.1 eV at the spot size of 400 μm. The obtained XPS spectrum was calibrated with C 1s peak (284.8 eV).

Electrochemical Measurements. All electrochemical experiments were conducted in a three-electrode system. Ag/AgCl/3 M NaCl and Pt plates were used as a reference electrode and a counter electrode, respectively. Electrochemical tests were carried out at room temperature using a potentiostat (CH Instruments 760E). 500 mM phosphate buffer (pH 7) was used as the electrolyte. The electrode potential *versus* Ag/AgCl was converted to the NHE scale, using the following equation: $E(\mathrm{NHE}) = E(\mathrm{Ag/AgCl}) + 0.197$ V. Additionally, the overpotential values were calculated by the difference between the *iR*-corrected potential ($V = V_{applied} - iR$) and the thermodynamic potential of water oxidation. Prior to every CV measurement, the solution resistance was measured and all the data were *iR*-compensated. Scan rate for all the CV curves was 0.05 V/s. The EIS was observed in the frequency range from 10^{-1} to 10^5 Hz with a 5 mV amplitude. During analysis, the electrolyte was mildly stirred by a magnetic bar to remove the oxygen bubbles on the surface of the electrodes.

■ ASSOCIATED CONTENT

Supporting Information

The Supporting Information is available free of charge at https://pubs.acs.org/doi/10.1021/acsomega.1c02397.

SEM, XPS, Raman, TEM, XANES, and EIS images (PDF)

■ AUTHOR INFORMATION

Corresponding Authors

Hyacinthe Randriamahazaka − *ITODYS, UMR 7086 CNRS, SIELE Group, Université Paris Diderot, Paris 75013, France; Chemistry, Université Paris Diderot, Paris 75205, France*; Email: hyacinthe.randria@univ-paris-diderot.fr

Ki Tae Nam − *Department of Materials Science and Engineering, Seoul National University, Seoul 08826, Republic of Korea; Nano System Institute, Seoul National University, Seoul 08826, Republic of Korea*; orcid.org/0000-0001-6353-8877; Email: nkitae@snu.ac.kr

Authors

Hongmin Seo − *Department of Materials Science and Engineering, Seoul National University, Seoul 08826, Republic of Korea*

Sunghak Park − *Department of Materials Science and Engineering, Seoul National University, Seoul 08826, Republic of Korea; Nano System Institute, Seoul National University, Seoul 08826, Republic of Korea*; orcid.org/0000-0001-9394-4833

Kang Hee Cho − *Department of Materials Science and Engineering, Seoul National University, Seoul 08826, Republic of Korea*

Seungwoo Choi − *Department of Materials Science and Engineering, Seoul National University, Seoul 08826, Republic of Korea*

Changwan Ko − *Department of Materials Science and Engineering, Seoul National University, Seoul 08826, Republic of Korea*

Complete contact information is available at: https://pubs.acs.org/10.1021/acsomega.1c02397

Author Contributions

⊥H.S., S.P., and K.H.C. contributed equally. The manuscript was written through contributions of all authors. All authors have given approval to the final version of the manuscript.

Notes

The authors declare no competing financial interest.

■ ACKNOWLEDGMENTS

This research was supported by Creative Materials Discovery Program through the National Research Foundation of Korea (NRF) funded by Ministry of Science and ICT (NRF-

2017M3D1A1039377), and Korea Environment Industry & Technology Institute (KEITI) through the Ecological Imitation-based Environmental Pollution Management Technology Development Project funded by Korea Ministry of Environment (MOE) (2021002800009). K.T.N. appreciates the support from Institute of Engineering Research, Research Institute of Advanced Materials (RIAM) and Soft Foundry at Seoul National University. H.R. acknowledges Université de Paris and CNRS for the support. S.P. appreciates the support from the POSCO Science Fellowship of POSCO TJ Park Foundation.

REFERENCES

(1) Dresselhaus, M. S.; Thomas, I. L. Alternative energy technologies. *Nature* **2001**, *414*, 332−337.
(2) Jiao, Y.; Zheng, Y.; Jaroniec, M.; Qiao, S. Z. Design of electrocatalysts for oxygen- and hydrogen-involving energy conversion reactions. *Chem. Soc. Rev.* **2015**, *44*, 2060−2086.
(3) Seh, Z. W.; Kibsgaard, J.; Dickens, C. F.; Chorkendorff, I.; Nørskov, J. K.; Jaramillo, T. F. Combining theory and experiment in electrocatalysis: Insights into materials design. *Science* **2017**, *355*, No. eaad4998.
(4) Shan, J.; Guo, C.; Zhu, Y.; Chen, S.; Song, L.; Jaroniec, M.; Zheng, Y.; Qiao, S.-Z. Charge-Redistribution-Enhanced Nanocrystalline Ru@IrOx Electrocatalysts for Oxygen Evolution in Acidic Media. *Chem* **2019**, *5*, 445−459.
(5) Gao, J.; Xu, C.-Q.; Hung, S.-F.; Liu, W.; Cai, W.; Zeng, Z.; Jia, C.; Chen, H. M.; Xiao, H.; Li, J.; Huang, Y.; Liu, B. Breaking Long-Range Order in Iridium Oxide by Alkali Ion for Efficient Water Oxidation. *J. Am. Chem. Soc.* **2019**, *141*, 3014−3023.
(6) Kanan, M. W.; Nocera, D. G. In Situ Formation of an Oxygen-Evolving Catalyst in Neutral Water Containing Phosphate and Co^{2+}. *Science* **2008**, *321*, 1072−1075.
(7) Huynh, M.; Bediako, D. K.; Nocera, D. G. Functionally Stable Manganese Oxide Oxygen Evolution Catalyst in Acid. *J. Am. Chem. Soc.* **2014**, *136*, 6002−6010.
(8) Guo, C.; Zheng, Y.; Ran, J.; Xie, F.; Jaroniec, M.; Qiao, S. Z. Engineering High-Energy Interfacial Structures for High-Performance Oxygen-Involving Electrocatalysis. *Angew. Chem., Int. Ed.* **2017**, *56*, 8539−8543.
(9) McCrory, C. C. L.; Jung, S.; Ferrer, I. M.; Chatman, S. M.; Peters, J. C.; Jaramillo, T. F. Benchmarking Hydrogen Evolving Reaction and Oxygen Evolving Reaction Electrocatalysts for Solar Water Splitting Devices. *J. Am. Chem. Soc.* **2015**, *137*, 4347−4357.
(10) Hunter, B. M.; Gray, H. B.; Müller, A. M. Earth-Abundant Heterogeneous Water Oxidation Catalysts. *Chem. Rev.* **2016**, *116*, 14120−14136.
(11) Man, I. C.; Su, H. Y.; Calle-Vallejo, F.; Hansen, H. A.; Martínez, J. I.; Inoglu, N. G.; Kitchin, J.; Jaramillo, T. F.; Nørskov, J. K.; Rossmeisl, J. Universality in Oxygen Evolution Electrocatalysis on Oxide Surfaces. *ChemCatChem* **2011**, *3*, 1159−1165.
(12) Suntivich, J.; May, K. J.; Gasteiger, H. A.; Goodenough, J. B.; Shao-Horn, Y. A Perovskite Oxide Optimized for Oxygen Evolution Catalysis from Molecular Orbital Principles. *Science* **2011**, *334*, 1383−1385.
(13) Busch, M.; Ahlberg, E.; Panas, I. Water Oxidation on MnO_x and IrO_x: Why Similar Performance? *J. Phys. Chem. C* **2013**, *117*, 288−292.
(14) Exner, K. S. Why approximating electrocatalytic activity by a single free-energy change is insufficient. *Electrochim. Acta* **2021**, *375*, 137975.
(15) Bediako, D. K.; Costentin, C.; Jones, E. C.; Nocera, D. G.; Savéant, J.-M. Proton−Electron Transport and Transfer in Electrocatalytic Films. Application to a Cobalt-Based O_2-Evolution Catalyst. *J. Am. Chem. Soc.* **2013**, *135*, 10492−10502.
(16) Morales-Guio, C. G.; Liardet, L.; Hu, X. Oxidatively Electrodeposited Thin-Film Transition Metal (Oxy)hydroxides as Oxygen Evolution Catalysts. *J. Am. Chem. Soc.* **2016**, *138*, 8946−8957.
(17) Kwon, G.; Jang, H.; Lee, J.-S.; Mane, A.; Mandia, D. J.; Soltau, S. R.; Utschig, L. M.; Martinson, A. B. F.; Tiede, D. M.; Kim, H.; Kim, J. Resolution of Electronic and Structural Factors Underlying Oxygen-Evolving Performance in Amorphous Cobalt Oxide Catalysts. *J. Am. Chem. Soc.* **2018**, *140*, 10710−10720.
(18) Lee, M. Y.; Ha, H.; Cho, K. H.; Seo, H.; Park, S.; Lee, Y. H.; Kwon, S.-J.; Nam, K. T.; Nam, K. T. Importance of Interfacial Band Structure between the Substrate and Mn_3O_4 Nanocatalysts during Electrochemical Water Oxidation. *ACS Catal.* **2019**, *10*, 1237−1245.
(19) Dau, H.; Limberg, C.; Reier, T.; Risch, M.; Roggan, S.; Strasser, P. The Mechanism of Water Oxidation: From Electrolysis via Homogeneous to Biological Catalysis. *ChemCatChem* **2010**, *2*, 724−761.
(20) Pham, H. H.; Cheng, M.-J.; Frei, H.; Wang, L.-W. Surface Proton Hopping and Fast-Kinetics Pathway of Water Oxidation on Co_3O_4 (001) Surface. *ACS Catal.* **2016**, *6*, 5610−5617.
(21) Wang, L.-P.; Van Voorhis, T. Direct-Coupling O_2 Bond Forming a Pathway in Cobalt Oxide Water Oxidation Catalysts. *J. Phys. Chem. Lett.* **2011**, *2*, 2200−2204.
(22) Nong, H. N.; Falling, L. J.; Bergmann, A.; Klingenhof, M.; Tran, H. P.; Spöri, C.; Mom, R.; Timoshenko, J.; Zichittella, G.; Knop-Gericke, A.; Piccinin, S.; Pérez-Ramírez, J.; Cuenya, B. R.; Schlögl, R.; Strasser, P.; Teschner, D.; Jones, T. E. Key role of chemistry versus bias in electrocatalytic oxygen evolution. *Nature* **2020**, *587*, 408−413.
(23) Naito, T.; Shinagawa, T.; Nishimoto, T.; Takanabe, K. Recent advances in understanding oxygen evolution reaction mechanisms over iridium oxide. *Inorg. Chem. Front.* **2021**, *8*, 2900−2917.
(24) Ooka, H.; Takashima, T.; Yamaguchi, A.; Hayashi, T.; Nakamura, R. Element strategy of oxygen evolution electrocatalysis based on in situ spectroelectrochemistry. *Chem. Commun.* **2017**, *53*, 7149−7161.
(25) Park, S.; Lee, Y. H.; Choi, S.; Seo, H.; Lee, M. Y.; Balamurugan, M.; Nam, K. T. Manganese oxide-based heterogeneous electrocatalysts for water oxidation. *Energy Environ. Sci.* **2020**, *13*, 2310−2340.
(26) Suga, M.; Akita, F.; Hirata, K.; Ueno, G.; Murakami, H.; Nakajima, Y.; Shimizu, T.; Yamashita, K.; Yamamoto, M.; Ago, H.; Shen, J.-R. Native structure of photosystem II at 1.95 Å resolution viewed by femtosecond X-ray pulses. *Nature* **2015**, *517*, 99−103.
(27) Zhang, B.; Sun, L. Why nature chose the Mn_4CaO_5 cluster as water-splitting catalyst in photosystem II: a new hypothesis for the mechanism of O−O bond formation. *Dalton Trans.* **2018**, *47*, 14381−14387.
(28) Retegan, M.; Krewald, V.; Mamedov, F.; Neese, F.; Lubitz, W.; Cox, N.; Pantazis, D. A. A five-coordinate Mn(IV) intermediate in biological water oxidation: spectroscopic signature and a pivot mechanism for water binding. *Chem. Sci.* **2016**, *7*, 72−84.
(29) Takashima, T.; Hashimoto, K.; Nakamura, R. Mechanisms of pH-Dependent Activity for Water Oxidation to Molecular Oxygen by MnO_2 Electrocatalysts. *J. Am. Chem. Soc.* **2012**, *134*, 1519−1527.
(30) Takashima, T.; Hashimoto, K.; Nakamura, R. Inhibition of Charge Disproportionation of MnO_2 Electrocatalysts for Efficient Water Oxidation under Neutral Conditions. *J. Am. Chem. Soc.* **2012**, *134*, 18153−18156.
(31) Zaharieva, I.; Chernev, P.; Risch, M.; Klingan, K.; Kohlhoff, M.; Fischer, A.; Dau, H. Electrosynthesis, functional, and structural characterization of a water-oxidizing manganese oxide. *Energy Environ. Sci.* **2012**, *5*, 7081−7089.
(32) Huynh, M.; Shi, C.; Billinge, S. J. L.; Nocera, D. G. Nature of Activated Manganese Oxide for Oxygen Evolution. *J. Am. Chem. Soc.* **2015**, *137*, 14887−14904.
(33) Zhang, B.; Chen, H.; Daniel, Q.; Philippe, B.; Yu, F.; Valvo, M.; Li, Y.; Ambre, R. B.; Zhang, P.; Li, F.; Rensmo, H.; Sun, L. Defective and "c-Disordered" Hortensia-like Layered MnO_x as an Efficient Electrocatalyst for Water Oxidation at Neutral pH. *ACS Catal.* **2017**, *7*, 6311−6322.
(34) Jin, K.; Chu, A.; Park, J.; Jeong, D.; Jerng, S. E.; Sim, U.; Jeong, H.-Y.; Lee, C. W.; Park, Y.-S.; Yang, K. D.; Kumar Pradhan, G.; Kim, D.; Sung, N.-E.; Hee Kim, S.; Nam, K. T. Partially Oxidized Sub-10

https://doi.org/10.1021/acsomega.1c02397
ACS Omega 2021, 6, 18404−18413

nm MnO Nanocrystals with High Activity for Water Oxidation Catalysis. *Sci. Rep.* **2015**, *5*, 10279.
(35) Cho, K. H.; Seo, H.; Park, S.; Lee, Y. H.; Lee, M. Y.; Cho, N. H.; Nam, K. T. Uniform, Assembled 4 nm Mn_3O_4 Nanoparticles as Efficient Water Oxidation Electrocatalysts at Neutral pH. *Adv. Funct. Mater.* **2020**, *30*, 1910424.
(36) Jin, K.; Seo, H.; Hayashi, T.; Balamurugan, M.; Jeong, D.; Go, Y. K.; Hong, J. S.; Cho, K. H.; Kakizaki, H.; Bonnet-Mercier, N.; Kim, M. G.; Kim, S. H.; Nakamura, R.; Nam, K. T. Mechanistic Investigation of Water Oxidation Catalyzed by Uniform, Assembled MnO Nanoparticles. *J. Am. Chem. Soc.* **2017**, *139*, 2277−2285.
(37) Cho, K. H.; Park, S.; Seo, H.; Choi, S.; Lee, M. Y.; Ko, C.; Nam, K. T. Capturing Manganese Oxide Intermediates in Electrochemical Water Oxidation at Neutral pH by In Situ Raman Spectroscopy. *Angew. Chem., Int. Ed.* **2021**, *60*, 4673−4681.
(38) Seo, H.; Jin, K.; Park, S.; Cho, K. H.; Ha, H.; Lee, K.-G.; Lee, Y. H.; Nguyen, D. T.; Randriamahazaka, H.; Lee, J.-S.; Nam, K. T. Mechanistic Investigation with Kinetic Parameters on Water Oxidation Catalyzed by Manganese Oxide Nanoparticle Film. *ACS Sustainable Chem. Eng.* **2019**, *7*, 10595−10604.
(39) Ramírez, A.; Hillebrand, P.; Stellmach, D.; May, M. M.; Bogdanoff, P.; Fiechter, S. Evaluation of MnOx, Mn_2O_3, and Mn_3O_4 Electrodeposited Films for the Oxygen Evolution Reaction of Water. *J. Phys. Chem. C* **2014**, *118*, 14073−14081.
(40) Tian, Z.-Y.; Mountapmbeme Kouotou, P.; Bahlawane, N.; Tchoua Ngamou, P. H. Synthesis of the Catalytically Active Mn_3O_4 Spinel and Its Thermal Properties. *J. Phys. Chem. C* **2013**, *117*, 6218−6224.
(41) Davi, M.; Mann, M.; Ma, Z.; Schrader, F.; Drichel, A.; Budnyk, S.; Rokicinska, A.; Kustrowski, P.; Dronskowski, R.; Slabon, A. An MnNCN-Derived Electrocatalyst for CuWO4 Photoanodes. *Langmuir* **2018**, *34*, 3845−3852.
(42) Doyle, R. L.; Godwin, I. J.; Brandon, M. P.; Lyons, M. E. G. Redox and Electrochemical Water Splitting Catalytic Properties of Hydrated Metal Oxide Modified Electrodes. *Phys. Chem. Chem. Phys.* **2013**, *15*, 13737−13783.
(43) Bard, A. J.; Faulkner, L. *Electrochemical Methods: Fundamentals and Applications*, 2nd ed.; Wiley: New York, 2001.
(44) Lee, J. W.; Hall, A. S.; Kim, J.-D.; Mallouk, T. E. Facile and Template-Free Hydrothermal Synthesis of Mn_3O_4 Nanorods on Graphene Sheets for Supercapacitor Electrodes with Long Cycle Stability. *Chem. Mater.* **2012**, *24*, 1158−1164.
(45) Augustyn, V.; Simon, P.; Dunn, B. Pseudocapacitive oxide materials for high-rate electrochemical energy storage. *Energy Environ. Sci.* **2014**, *7*, 1597−1614.
(46) Jamnik, J.; Maier, J. Generalised equivalent circuits for mass and charge transport: chemical capacitance and its implications. *Phys. Chem. Chem. Phys.* **2001**, *3*, 1668−1678.
(47) Jang, J. H.; Oh, S. M. Complex Capacitance Analysis of Porous Carbon Electrodes for Electric Double-Layer Capacitors. *J. Electrochem. Soc.* **2004**, *151*, A571.
(48) Randriamahazaka, H.; Asaka, K. Electromechanical Analysis by Means of Complex Capacitance of Bucky-Gel Actuators Based on Single-Walled Carbon Nanotubes and an Ionic Liquid. *J. Phys. Chem. C* **2010**, *114*, 17982−17988.
(49) Schönleber, M.; Ivers-Tiffée, E. The Distribution Function of Differential Capacity as a new tool for analyzing the capacitive properties of Lithium-Ion batteries. *Electrochem. Commun.* **2015**, *61*, 45−48.
(50) Bisquert, J.; Bertoluzzi, L.; Mora-Sero, I.; Garcia-Belmonte, G. Theory of Impedance and Capacitance Spectroscopy of Solar Cells with Dielectric Relaxation, Drift-Diffusion Transport, and Recombination. *J. Phys. Chem. C* **2014**, *118*, 18983−18991.
(51) Hasyim, M. R.; Rajagopalan, R. Prediction of Discharge Performances of Pseudocapacitors Using Their Impedance Characteristics. *J. Electrochem. Soc.* **2020**, *167*, 013536.

https://doi.org/10.1021/acsomega.1c02397
ACS Omega 2021, 6, 18404−18413